



Deposited via The University of Leeds.

White Rose Research Online URL for this paper:

<https://eprints.whiterose.ac.uk/id/eprint/141227/>

Version: Accepted Version

Article:

Bradley, D, Lawes, M and Morsy, ME (2019) Flame speed and particle image velocimetry measurements of laminar burning velocities and Markstein numbers of some hydrocarbons. *Fuel*, 243. pp. 423-432. ISSN: 0016-2361

<https://doi.org/10.1016/j.fuel.2019.01.067>

© 2019 Elsevier Ltd. All rights reserved. This manuscript version is made available under the CC-BY-NC-ND 4.0 license <http://creativecommons.org/licenses/by-nc-nd/4.0/>.

Reuse

This article is distributed under the terms of the Creative Commons Attribution-NonCommercial-NoDerivs (CC BY-NC-ND) licence. This licence only allows you to download this work and share it with others as long as you credit the authors, but you can't change the article in any way or use it commercially. More information and the full terms of the licence here: <https://creativecommons.org/licenses/>

Takedown

If you consider content in White Rose Research Online to be in breach of UK law, please notify us by emailing eprints@whiterose.ac.uk including the URL of the record and the reason for the withdrawal request.

1 Flame Speed and Particle Image Velocimetry Measurements of
2 Laminar Burning Velocities and Markstein Numbers of some
3 Hydrocarbons.

4 D. Bradley*, M. Lawes, M. E. Morsy

5 *School of Mechanical Engineering, University of Leeds, Leeds LS2 9JT, UK.*

6 **Corresponding author: D.Bradley@leeds.ac.uk*

7
8 **Abstract**

9 Particle Image Velocimetry, PIV, is described for measuring laminar burning velocities during flame propagation
10 in spherical explosions, by the measurement of the flame speed and gas velocity just ahead of the flame.
11 Measurements made in this way are compared with those obtained from the flame speed method, which is based
12 on the flame front propagation speed and the ratio of unburned to burned gas densities. Different values arise
13 between the two methods, and the principal reason is the common assumption in the flame speed method that the
14 burned gas density is at the equilibrium, burned gas, adiabatic temperature. When allowance is made for the effects
15 of flame stretch rate and Lewis number on this density, the differences in burning velocities are significantly
16 decreased. The PIV methodology enables mass rate of burning velocities to be expressed in terms of the burning
17 velocity at zero stretch rate and the Markstein numbers for strain rate and flame curvature. Burning velocities and
18 Markstein numbers are presented for methane, *i*-octane, ethanol, and *n*-butanol over a range of equivalence ratios
19 at atmospheric pressure and, in the case of *n*-butanol, also over a range of pressures. Account is taken of the low
20 stretch rate at which a laminar flame becomes unstable, and, below which, the burn rate increases due to the
21 enhanced flame surface area. The critical stretch rates for the transition are identified. In measuring Markstein
22 numbers, there is a dependency upon the isotherm employed for the measurement of the stretch rate. This aspect
23 is studied by comparing measurements with two different isotherms. It is concluded that the measured PIV
24 flame measurements might under-estimate the Markstein numbers by about 12%.

25 *Keywords: Laminar burning velocity; Flame instability; Markstein numbers; spherical explosion flames.*

27	Nomenclature		55		
28	A	m^2	flame surface area	56	S_n m/s stretched laminar flame speed
29	c_p	J/kg.K	specific heat	57	S_s m/s unstretched laminar flame speed
30	D	m^2/s	thermal diffusivity ($\lambda/\rho C_p$)	58	t s time
31	D_{im}	m^2/s	minority species diffusion	59	T_b K adiabatic equilibrium burned gas
32			coefficient	60	temperature
33	K		Karlovitz stretch factor	61	\bar{T}_b K burned gas mean temperature
34			$(\delta \alpha_{sr}/u_l + \delta \alpha_{cr}/u_l)$	62	T_u K unburned gas temperature
35	K_{cl}		critical Karlovitz number	63	u_g m/s outwards gas velocity
36	K_c, K_s		Karlovitz curvature and strain	64	u_l m/s PIV, unstretched laminar burning
37			rate factors, $(\delta \alpha_{cr}/u_l), (\delta \alpha_{sr}/u_l)$	65	velocity, u_n at $\alpha = 0$
38	L_b	m	flame speed Markstein length	66	u_{la} m/s adiabatic density, unstretched laminar
39	L_{cr}, L_{sr}	m	curvature and strain Markstein	67	burning velocity, see Eq. (5)
40			lengths, respectively, associated	68	u_{lr} m/s PIV u_l with no radiative loss
41			with u_{nr}	69	u_{ls} m/s density corrected, unstretched laminar
42	L_u	m	Markstein length for u_n	70	burning velocity, $\rho_b = \bar{\rho}_b$ in Eq.(5) and
43	Le		Lewis number ($\lambda/\rho D_{im} c_p$)	71	$u_{ls} = u_{la}$
44	Ma		Markstein number	72	u_n m/s flame entrainment laminar velocity
45	Ma_b		flame speed Markstein number	73	u_{nr} m/s stretched laminar mass burning velocity
46	Ma_{cr}, Ma_{sr}		curvature and strain Markstein	74	expressing mass burning rate
47			numbers, respectively, associated	75	, see Eqs. (7) and (8).
48			with u_{nr}	76	Greek Symbols
49	P	Pa	initial pressure	77	α 1/s flame stretch rate
50	Pe_{cl}		critical Peclet number, r_{cl}/δ	78	α_{cl} 1/s critical stretch rate for flame
51	Pr		Prandtl number ($c_p \eta / \lambda$)	79	instability
52	r_{cl}	m	critical flame radius	80	α_{cr} 1/s curvature strain rate
53	r_u	m	cold flame front radius	81	α_{sr} 1/s strain rate
54	S		flame speed factor, Eq. (4)	82	γ ratio of specific heats

83	δ	m	flame thickness ($(\nu/u_l)/Pr$)	87	φ		equivalence ratio
84	λ	J/m.K.s	thermal conductivity	88	ρ_b	kg/m ³	adiabatic-burned gas density
85	μ	kg/m.s	dynamic viscosity	89	$\bar{\rho}_b$	kg/m ³	mean burned gas density
86	ν	m ² /s	kinematic viscosity	90	ρ_u	kg/m ³	unburned gas density

91 1. Introduction

92 An early critical review of laminar burning velocity, u_l , described six different measurement techniques, including
93 particle tracking, for measuring velocities, yet it omitted any treatment of flame stretch rate [1]. At an early stage,
94 it became apparent that more complete data on flow velocities, from particle tracking [2] and hot wire anemometry
95 [3], yielded values of u_l that differed from those obtained from more traditional techniques. Later, Direct
96 Numerical Simulations [4] showed that burning velocities based solely upon schlieren measurements of flame
97 speeds in strongly radiating spherical explosion flames would be under-predicted, and would be more accurately
98 measured with particle image velocimetry, PIV.

99 Yufei Dong et al. [5] employed PIV in the flow configuration ahead of a stagnation plate, whilst Balusamy et al.
100 [6] employed it to measure the laminar burning velocities of propane/air mixtures in spherical explosion flames.
101 Varea et al. [7] also used such flames to measure laminar burning velocities and Markstein lengths of methane,
102 ethanol and *i*-octane/air. Measurements of laminar burning velocity by this technique are not widespread because
103 of the inherent experimental difficulties and necessary post-processing of a large number of data points. As a
104 result, the spherical flame explosion technique, based solely on flame speed measurements, has become widely
105 employed for this purpose. This flame speed method necessitates assumptions about the adiabatic density of the
106 burned gas that are not required with PIV, which simultaneously measures the flame speed and gas velocity just
107 ahead of the flame. The difference in these values gives a burning velocity that can yield a mass rate of burning.
108 In addition, both the flame curvature and strain rate contributions to the flame stretch rate, α , can readily be found.

109 The present paper reports PIV measurements in spherical explosions, from which burning velocities can also be
110 derived from the flame speed measurements. The velocity measurements also enable entrainment and mass rate
111 of burning velocities to be found, along with flame stretch rates and associated Markstein numbers. In the flame
112 speed method of measuring burning velocity, it is often assumed that the burned gas density at zero stretch rate is
113 that of an adiabatic flame under equilibrium conditions, ρ_b . This tends to be an under-estimation, giving burning
114 velocities that are shown to be about 4-11 % low. A modification of this approach is developed, involving the
115 burned gas density of the stretched flame, entirely in the regime of stable propagation, prior to the development

116 of unstable flames at low stretch rate. In the stable regime, the mean burned gas density, $\bar{\rho}_b$, is larger than ρ_b , and
 117 depends on the stretch rate, α , and Lewis number, Le . There is little change in $\bar{\rho}_b$ before the instability develops.
 118 Values of $\bar{\rho}_b$ yield values of burning velocities that are closer to those determined by PIV. The PIV method
 119 provides more complete information on flame propagation and, consequently, more accurate data on burning
 120 velocities, the influences of flame stretch rates, the onset of flame instabilities, and radiative energy exchanges.
 121 Burning velocities are presented from both of the flame speed methods, as well as the PIV-derived values for
 122 methane, *n*-butanol, *i*-octane and ethanol mixtures with air and, in the case of *n*-butanol, over a range of pressures.
 123 The paper develops a methodology for correcting burning velocities, measured by the flame speed method, due
 124 to it not having an adiabatic value for the burned gas density. Normal strain rate laws and Markstein numbers are
 125 only applicable during the propagation of stable flames and a methodology for defining this regime is explained.
 126 Errors arise in the determination of Markstein numbers, if the temperature of the associated isotherm is too low,
 127 and this effect is quantified.

128 2. PIV velocities, flame speeds, stretch rates and Markstein numbers

129 The basic PIV velocities are related by:

$$130 \quad u_n = S_n - u_g . \quad (1)$$

131 Here u_n is the stretched laminar entrainment velocity, S_n , the stretched flame speed, and u_g the maximum
 132 outwards gas velocity component, normal to the flame. The overall stretch rate, α , of a spherical explosion flame,
 133 of leading edge radius, r_u , is given by:

$$134 \quad \alpha = \frac{1}{A} \frac{dA}{dt} = \frac{2}{r_u} \frac{dr_u}{dt} = \frac{2}{r_u} S_n, \quad (2)$$

135 with $S_n = dr_u/dt$.

136 The flame entrainment velocity, u_n , is related to the flame speed, S_n , by [8]:

$$137 \quad u_n = \bar{\rho}_b S_n / \rho_u + r_u / (3\rho_u) (d\bar{\rho}_b / dt), \quad (3)$$

138 with $\bar{\rho}_b$, the mean density within the radius, r_u .

139 A stable flame takes time to develop from the initiating spark plasma. Whilst the flame is developing with a small
 140 radius, r_u , $\bar{\rho}_b$, is higher than the density of the adiabatically burned equilibrium gas, ρ_b , at a temperature, T_b .
 141 Measurements of u_n were only made, at constant pressure, after a stable flame had become established. With
 142 continuing flame growth, the final term in Eq. (3) decreases and finally becomes negligible. During this time, this
 143 changing condition is expressed by a flame speed factor:

$$144 \quad S = u_n \rho_u / S_n \rho_b. \quad (4)$$

145 S starts with a value of about 2 and diminishes towards unity as $\bar{\rho}_b$, in Eq. (3), decreases and approaches ρ_b [8].
 146 With the flame stretch rate approaching zero, the flame speed approaches a stretch-free value of S_s , with the
 147 burning velocity, u_{la} . Neglecting radiative heat transfer from the burned gas, its density at the adiabatic
 148 equilibrium temperature of, T_b , in Eq. (4) yields:

$$149 \quad S = 1 \text{ and a laminar burning velocity, } u_{la} = (\rho_b/\rho_u)S_s. \quad (5)$$

150 This expression is widely used in the flame speed method for measuring u_{la} . The flame speed, S_n , at a stretch
 151 rate α , is related to S_s by a flame speed Markstein length, L_b , in the relationship [9]:

$$152 \quad S_s - S_n = L_b \alpha. \quad (6)$$

153 The mass burning rate velocity, u_{nr} , at constant pressure for the formation of completely burned gas [10, 11] is
 154 related to u_n and S_n by [8]:

$$155 \quad u_{nr} = (S_n - u_n) \left(\frac{\rho_u}{\rho_b} - 1 \right)^{-1} = u_g \left(\frac{\rho_u}{\rho_b} - 1 \right)^{-1}, \quad (7)$$

156 There are two contributions to α , one due to strain rate, α_{sr} , $2u_g/r_u$, the other to flame curvature, α_{cr} , $2u_n/r_u$,
 157 with $\alpha = \alpha_{sr} + \alpha_{cr}$. Each has an associated Markstein length, L_{sr} and L_{cr} , and the influence of flame stretch rate
 158 upon the burning velocity is expressed by [8]:

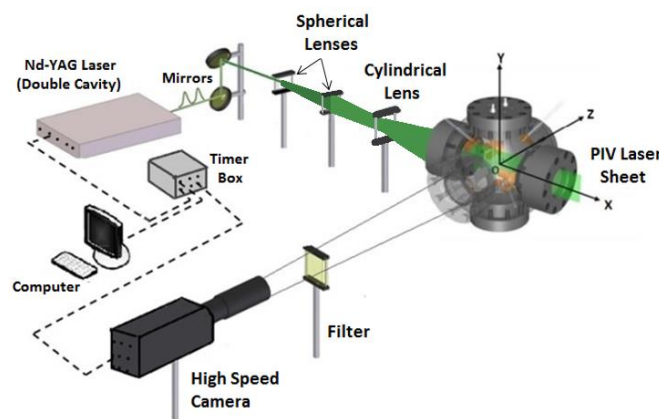
$$159 \quad u_l - u_{nr} = L_{sr}(2u_g/r_u) + L_{cr}(2u_n/r_u), \quad (8)$$

160 with u_l the stretch-free laminar burning velocity with $\alpha = 0$. Markstein numbers are obtained by normalising
 161 these lengths with the laminar flame thickness, given by $(\nu/u_l)/Pr$, where ν is the mixture kinematic viscosity,
 162 and Pr the Prandtl number, both obtained at the unburned gas temperature using the Gaseq code [12]. Also for
 163 the derivation of accurate Markstein lengths, the isotherm upon which α is based in Eq. (2) should be closer to
 164 the burned gas, than to the unburned gas temperature [13].

165 **3. Apparatus**

166 Measurements of S_n and u_g were made in spherical explosion flames at 0.1 MPa for methane, *i*-octane and
 167 ethanol/air mixtures at 300 K, 358 K and 360 K, respectively, over a range of equivalence ratios, and also for *n*-
 168 butanol/air mixtures at 383 K between 0.1 and 0.5 MPa. The explosions occurred in a spherical stainless steel
 169 explosion vessel of 190 mm inner radius. Flame images were obtained through three pairs of orthogonal windows
 170 of 150 mm diameter, enabling flame radii to be measured up to 60 mm, after a stable flame had been established
 171 at a radius of about 10 mm. An electric heater aided evaporation. Mixture temperatures were measured with a
 172 sheathed chromel–alumel thermocouple and mixing was facilitated by four fans, driven by electric motors, located
 173 close to the vessel wall [14].

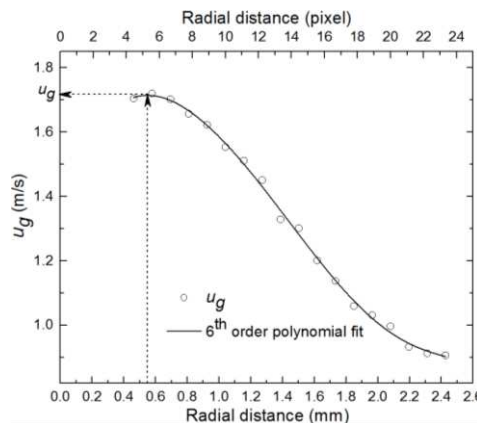
174 A double pulsed Nd:YAG laser (DM60-DH, Photonics), generated pulses of 12 mJ at a wavelength of 532 nm at
 175 5 KHz. These, created a sheet about 0.5 mm thick to illuminate the uniformly dispersed seeding particles in the
 176 flow. The laser beam was expanded into a vertical sheet in the middle of the explosion vessel, as indicated in Fig.
 177 1. The measuring system was comprised of two spherical lenses of -650 mm and 300 mm focal lengths and
 178 cylindrical lens of -20 mm focal length. A high-speed camera, perpendicular to the laser sheet, recorded a 12-bit
 179 image pair of 1024×1024 pixels at a frequency of 5 kHz. The camera was fitted with a macro-Nikon lens of 108
 180 mm focal length, coupled with an optical band pass filter centered at 532 nm to minimise the effect of flame
 181 luminosity. Six jet atomisers (9010F0021, DANTEC) generated olive oil droplets $< 1 \mu\text{m}$, with a boiling
 182 temperature of 570 K. The particle density was 0.51 (particles/pixel). Their evaporation defined the flame location
 183 as close to the 570 K isotherm. For comparison, in the widely used flame speed method, the flame is often located
 184 by a schlieren front. Based on the structure of a stoichiometric CH_4/air flame, this is approximately the 856 K
 185 isotherm [15].



186
 187 **Fig. 1.** Optical configuration.

188 Image analysis and the derivation of flame speed employed computational software developed by the Dantec
 189 Dynamics Company. The first stage identified the location of the flame edge, tracking its progression from one
 190 image to the next, using a phase boundary detection tool. The flame edge was first located and its progression
 191 tracked, by the evaporative disappearance of the oil particles, enhanced by increasing the contrast. The second
 192 step, corrected for unwanted light sheet non-uniformities. The burned gas boundary was located with sub-pixel
 193 resolution. The detected flame edges were smoothed by a low pass filter to remove noise from the digitisation
 194 steps and a least squares algorithm calculated the best fit circle to the flame edge and the corresponding flame
 195 radius. The flame speed, associated with the 570 K isotherm, could then be found from the temporal evolution of
 196 the flame front.

197 Balusamy et al. [6] used an adaptive algorithm to measure directly the local, radially outwards, unburned gas
 198 velocity, at entry to the flame front. In the present work, an adaptive algorithm was employed within the Dantec
 199 software, in an Adaptive PIV Method. This is an iterative and automatic way of calculating velocity vectors, based
 200 on the seeding particle density. It assumes that all seeding particles evaporate completely at the iso-surface. The
 201 orientation of individual interrogation areas, IA, were iteratively adjusted to fit the local seeding densities and
 202 velocity gradients. The appropriate IA size was automatically determined for each individual IA, by specifying
 203 maximum and minimum size limits. A first iteration always used the largest IA size, which was reduced in
 204 subsequent iterations. This allowed reduction of IA sizes where the particle density was sufficiently high. The
 205 minimum IA determined the location and magnitude of vectors. This location was chosen to be associated with
 206 the edge of the minimum IA. This minimum IA employed 8 pixels along the flame front and 2 pixels in the normal
 207 direction to the flame ($0.86 \text{ mm} \times 0.21 \text{ mm}$), while the maximum was ($8 \times 8 \text{ pixels} \sim 0.86 \times 0.86 \text{ mm}$). To
 208 characterise the velocity profile ahead of the flame front, a sub-pixel tool was developed, linked to the Dantec
 209 software to achieve the value of the minimum IA with one pixel step. An example of an instantaneous gas velocity
 210 profile for a methane/air flame is presented in Fig. 2, in which zero distance locates the evaporation isotherm.



211

212 **Fig. 2.** Gas velocity ahead of flame, CH_4/air , $\phi = 1.0$, at 0.1 MPa, 300 K.

213 The maximum gas velocity, u_g , is obtained by fitting the velocity profile to a 6th order polynomial, which gives
 214 the highest value of R^2 . This maximum value is located about 2–8 pixels ($0.21\text{--}0.86 \text{ mm}$) ahead of the
 215 evaporation isotherm. Computational studies show a sharp change in gas velocity within the flame zone, with a
 216 much smaller variation ahead of the flame [10], as indicated by the profile of measured values, with the maximum
 217 value arrowed, in Fig. 2. This adaptive PIV method was used alongside a developed program to calculate the
 218 burning velocity. The program calculated the burning velocity from the flame edge profiles and the average value

219 of the maximum unburned gas velocity measurements. More details concerning the data processing are to be
220 found in the supplementary material [S1].

221 The temperature of 570 K, associated with the disappearance of the evaporating droplets, is probably too low for
222 a front that yields the value of the stretch rate, and a schlieren front close to 860K [15] is preferable. High speed
223 schlieren cine photography therefore was employed to study the effect of the isotherm on measurements of L_b .
224 The technique allows the visual detection of the flame front through the density gradients between the burned and
225 unburned mixtures, caused by the varying degrees of light refraction. A schematic figure of the schlieren optical
226 configuration can be found in the supplementary material [S2]. A near point source of light was provided by a 20
227 mW (regulated to 5mW), 635 nm LED laser. This expanded on to a f -1000 mm plano-convex lens, collimating
228 a 150 mm beam through the vessel and its contents to another f -1000 mm plano-convex lens. This focused the
229 beam on to a variable diameter iris (1-15 mm). The camera was positioned to give a field of view of 110 mm. This
230 took full advantage of the camera resolution of 1024×1024 pixels with ~ 0.11 mm/pixel. This resolution was more
231 than sufficient to capture a defined flame edge, whilst allowing an ample sampling rate of 5 kHz.

232 Figure 3 shows two flame images of an ethanol/air mixture, $\varphi = 0.8$, at 0.1 MPa and 360 K, recorded by both PIV
233 and schlieren techniques. The same image analysis and derivation of flame speed identified the flame edges,
234 shown by the white circles. A slight deformation of the flame can be observed, but this did not induce any
235 significant departure from sphericity. The near constant maximum gas velocity profile around the flame also
236 indicated that buoyancy effects were negligible.

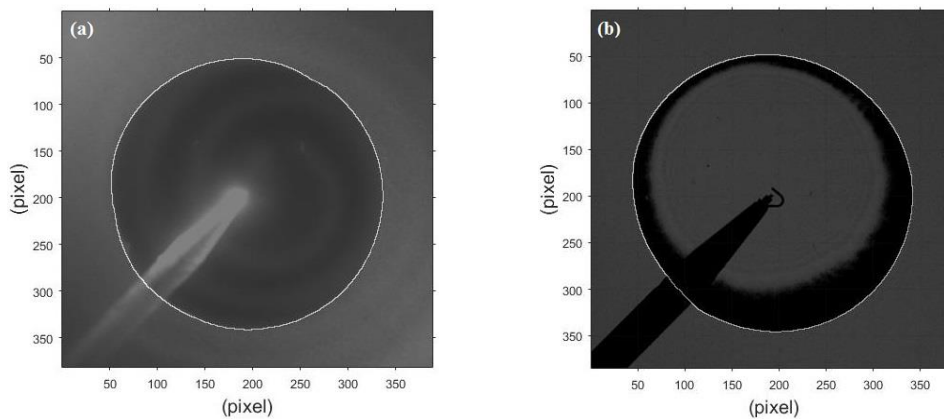
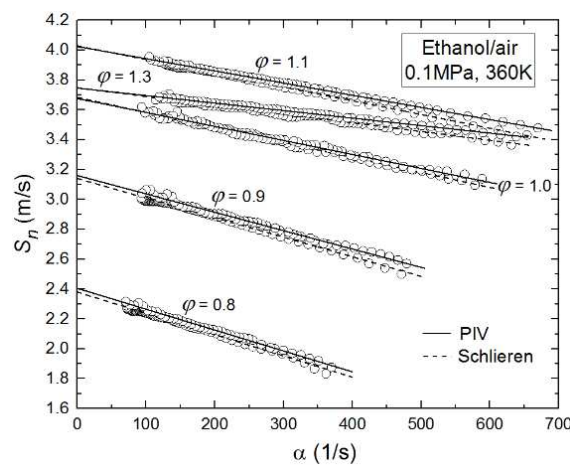


Fig. 3. Flame images of lean ethanol/air mixture, $\varphi=0.8$ at 0.1 MPa and 360 K. (a) PIV image, $\alpha =140.7$ (1/s) and $S_n=2.30$ m/s. (b) Schlieren image, $\alpha =144.2$ (1/s) and $S_n=2.18$ m/s. Scale (0.11 mm/pixel). White circles show flame edges.

237 4. Experimental methodology

238 4.1. Stretch rate isotherms

239 Flame speed, S_n , is plotted against the stretch rate, α , given by Eq. 2, from which the flame speed Markstein
240 length, L_b , is found using Eq. (6). The flame speed is almost independent of the chosen isotherm, but the flame
241 stretch rate also depends on the changing radius of the isotherm, see Eq. (2). An isotherm close to the temperature
242 of the burned gas might be regarded as closest to expressing the rate of formation of burned gas, akin to u_{nr} , Ma_{sr}
243 and Ma_{cr} [8]. Beeckmann et al. [16] showed that PIV and schlieren techniques yield nearly identical Markstein
244 lengths, for a methane/air mixture, $\phi = 1.1$ at 0.25 MPa and 298 K. Giannakopoulos et al. [13] showed isotherms
245 in the reaction zone to be more reliable than those in the preheat zone for measuring Markstein numbers.
246 Measured flame speeds from both the PIV and schlieren images, plotted against α , are compared in Fig. 4, for
247 C_2H_5OH /air flames at different equivalence ratios, ϕ , at 0.1 MPa, and an initial temperature of 360 K. Those based
248 on PIV Mie scattering images, shown by the full lines, are close to isotherms in the region of 570 K, in contrast
249 to the schlieren images, shown by the broken lines, corresponding to isotherms at about 860 K. As in [13], the
250 higher temperatures gives the higher L_b , between 4-12 % higher than the lower temperatures. For the same two
251 temperatures, but using the theoretical propane/air data in [13] the Markstein numbers would be 50-90% higher
252 at the higher temperature.



253 **Fig. 4.** Variations of PIV and schlieren S_n values with ϕ for ethanol/air mixtures at 0.1 MPa and 360 K. Full and
254 dashed lines denote linear relationship for L_b through PIV and schlieren points, respectively.
255

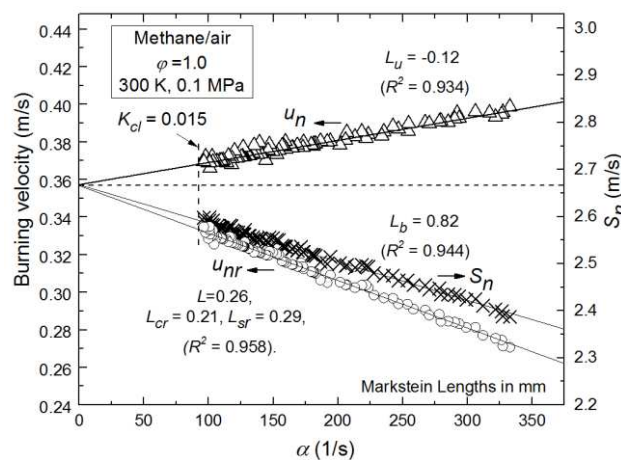
256 In [13] plateau temperatures are evaluated, at which there is no further change in Markstein number with isotherm
257 temperature. For the conditions in Fig. 4, a suitable plateau isotherm would be that at least 1440 K, ($4 \times T_u$). When
258 extrapolated to this temperature, values of L_b at 570 and 860 K give values of L_b between 5 and 18 % higher than
259 those measured at the seed disappearance isotherm, and 3-5% higher than those at the schlieren front. Throughout

260 the present study L_b is measured at the PIV droplet disappearance isotherm, and the underestimation is in the
 261 higher of the two ranges.

262 4.2. Stretch rate effects

263 The flame speed method of determining u_{la} employs Eq. (6), with S_n plotted against α , given by Eq. (2); S_n is
 264 extrapolated to zero stretch rate, where $S_n = S_s$, and $u_{la} = (\rho_b/\rho_u)S_s$. Figure 5 shows such a plot for CH₄/air, φ
 265 = 1.0, at 0.1 MPa and 300 K. Values on the y axes are so chosen that the horizontal dashed line in the figure shows
 266 S_s on the secondary S_n axis and u_{la} from Eq. (5) on the burning velocity axis, with ρ_b/ρ_u calculated from the
 267 Gaseq code [12]. Also plotted are PIV values of u_n from Eq. (1). Because S , and hence u_n/S_n , always decrease
 268 in an explosion, as S_n increases, u_n must decrease, as in the figure, and, from Eq. (7), u_{nr} must increase, also as
 269 shown.

270 Values of u_{nr} were found from PIV data using Eq. (7) and L_{sr} and L_{cr} by numerical iteration of the u_{nr} data. In
 271 a first iteration, L_{sr} and L_{cr} in Eq. (8) were assumed equal. This yielded an optimal value for this mixture of 0.26
 272 mm, labelled L in Fig. 5. Further iterations with separate values of L_{sr} and L_{cr} yielded the values given on the
 273 figure. The second iteration step plotted u_{nr} against α_{sr} and α_{cr} separately. This gave initial values of the
 274 corresponding L_{sr} and L_{cr} . The third step inserted these initial values into a program in which a series of iterations
 275 computed the associated values of u_{nr} from Eq. (8). These were sensitive to the combination of L_{sr} and L_{cr} . Those
 276 that gave the highest value of R^2 were adopted. These were $L_{sr} = 0.29$ mm and $L_{cr} = 0.21$ mm for methane/air
 277 mixtures, $\varphi = 1.0$, at 0.1 MPa and 300 K. This procedure was followed for all mixtures. Plots of $u_{nr} =$
 278 $u_g \left(\frac{\rho_u}{\rho_b} - 1 \right)^{-1}$, from Eq. (7) against α when extrapolated to $\alpha = 0$, yielded the PIV value of u_l in Eq. (8),
 279 appropriate to u_{nr} .



280
 281 **Fig. 5.** Variations of S_n , u_n , and u_{nr} with flame stretch rate methane/air mixtures, $\varphi = 1.0$, at 0.1 MPa and 300
 282 K. Dashed horizontal line links $u_n (= u_l)$ and $S_n (= S_s)$ in Eq. (5).

283 Although a value of L_u in, $u_l - u_n = L_u \alpha$, is given in Fig. 5, Eq. (3) shows u_n , is not a sole variable with α , but
 284 depends upon other factors. Only in the later stages does it become a true burning velocity. Because L_u lacks the
 285 consistency of a Markstein length, no attempt is made to feature it or evaluate its two components.

286 In Fig. 5, the validity of the two experimental lines is confined to the markers. At the early, higher, values of α
 287 the small radius flame has characteristics of both a spark plasma and developing reactions, before transformation
 288 into a flame. Low spark ignition energies were employed and the minimum flame radius was about 10 mm.
 289 Between this radius and the upper limit of 60 mm, depending upon the mixture, it was possible for Darius-Landau
 290 and thermo-diffusive instabilities to develop at a stretch rate, α_{cl} . The critical radius is r_c , and the critical Peclet
 291 number, r_c/δ , is Pe_{cl} . The cellular flame structure so created increases S_n [17, 18]. At this critical condition, the
 292 Karlovitz stretch factor, $K = \alpha \delta_l / u_l$ attains a critical condition, with $\alpha = \alpha_{cl}$, and is given by [19]:

$$293 \quad K_{cl} = (2\sigma/Pe_{cl})[1 + (2Ma_b/Pe_{cl})]^{-1}. \quad (9)$$

294 Instabilities develop at values of K less than this value.

295 The experimental values of S_n and u_n , plotted in Fig. 5, cover the entire stable regime. All values of K_{cl} are taken
 296 from the values for different fuel/air mixtures, in [20]. The corresponding stability limit, in terms of α , is indicated
 297 by the short vertical line, $K_{cl} = 0.015$ in Fig. 5. In some instances, just prior to the rapid increase in flame speed,
 298 values of S_n became oscillatory. Eq. (8) is the practical formulation of the mass rate of burning, but its validity
 299 does not extend into the regime of unstable flames, below α_{cl} down to the value of u_l at $\alpha = 0$, which is imaginary.

300 4.3. Burned gas density

301 Only if reaction has been completed adiabatically, is Eq. (5) valid. Clavin and Williams [21] show the value of
 302 burned gas density to be dependent upon α and the Lewis number, Le . The deviation of the mean burned gas
 303 temperature, \bar{T}_b , from the adiabatic burned gas temperature, T_b , is given [11,22] by:

$$304 \quad \frac{\bar{T}_b - T_b}{T_b} = \frac{D}{(u_{la})^2} \left(\frac{1}{Le} - 1 \right) \alpha. \quad (10)$$

305 Here, D , is the thermal diffusivity of the mixture, obtained, like T_b , from [12], for the initial conditions of T_u and
 306 P . Measurements of temperature distributions have confirmed the general validity of this equation [11,22]. It
 307 shows that high α and Le values can, under some circumstances, create mean temperatures significantly below
 308 adiabatic values. As α decreases the temperature slowly recovers, but only with $Le = 1.0$ can $\bar{T}_b = T_b$. The
 309 changes in α are known, as the flame radius increases during the period of flame stability. Figures 6 and 7, derived
 310 from this equation, show \bar{T}_b and $\bar{\rho}_b$ plotted against flame radius, r_u . For the stoichiometric CH_4 mixture of Fig. 6

311 with $Le = 0.99$ [23, 24] and $D = 2.01 \times 10^{-5} \text{ m}^2/\text{s}$ [12], the figure shows the near unity value of Le ensures early
 312 attainment of the adiabatic equilibrium values, T_b and ρ_b , in accordance with Eq. (5). This explains the good
 313 convergence of the S_n and u_n straight lines at $\alpha = 0$ in Fig. 5, giving $u_l = u_{la} = 0.358 \pm 0.005 \text{ m/s}$.

314 In sharp contrast, is the stoichiometric $n\text{-C}_4\text{H}_9\text{OH}$ mixture at 383 K and 0.1 MPa, with $Le = 1.58$ [25] and $D =$
 315 $2.72 \times 10^{-5} \text{ m}^2/\text{s}$ [12]. Here the high Le ensures \bar{T}_b does not attain T_b in Fig.7, and $\bar{\rho}_b > \rho_b$. Figure 8 shows
 316 data for the same mixture, but with \bar{T}_b and $\bar{\rho}_b$ at 0.5 MPa, $Le = 1.12$ and $D = 5.6 \times 10^{-6} \text{ m}^2/\text{s}$ [12]. The figure
 317 shows the increase in pressure to lead to a rather more rapid attainment of adiabatic equilibrium, attributable to
 318 the decreases in both Le and D .

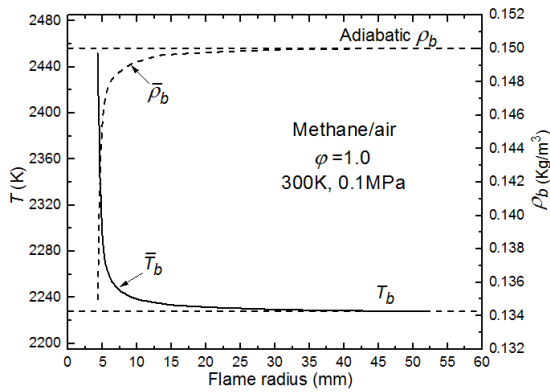


Fig. 6. Computed burned gas temperature and density CH_4/air , $\phi = 1.0$, at 300 K and 0.1 MPa, $Le = 0.991$.

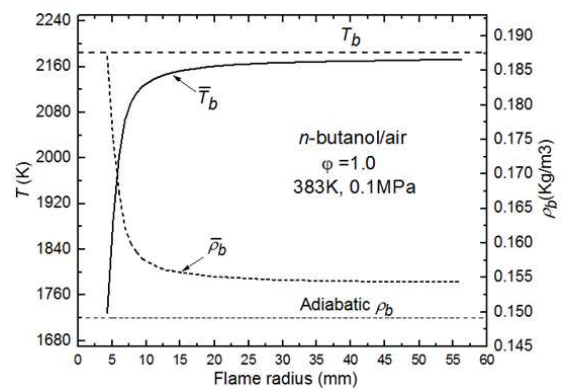


Fig. 7. Computed burned gas temperature and density for $n\text{-C}_4\text{H}_9\text{OH}/\text{air}$, $\phi = 1.0$ at 383 K and 0.1 MPa, $Le = 1.58$.

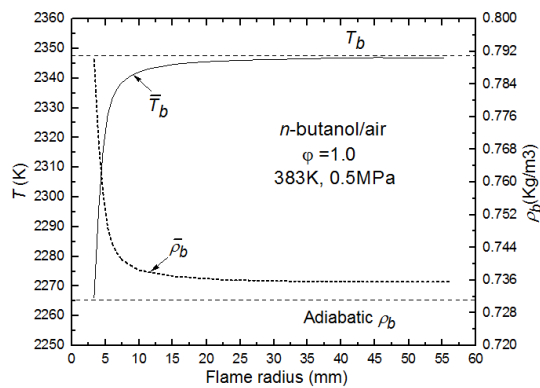


Fig. 8. Computed burned gas temperature and density for $n\text{-C}_4\text{H}_9\text{OH}/\text{air}$, $\phi = 1.0$ at 383 K and 0.5 MPa, $Le = 1.12$.

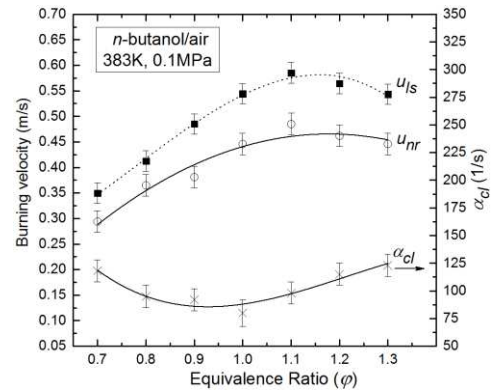


Fig. 9. PIV values of u_{nr} at the boundary values of critical stretch rate, α_{cl} , and values of u_{ls} for $n\text{-butanol}/\text{air}$ at 0.1 MPa and 383 K.

319 Mean values, $\bar{\rho}_b$, within the stable extrapolation range of S_n , were found in this manner during explosions. There
 320 is little change in $\bar{\rho}_b$ during the developed stable flame propagation. To find the stretch-free value of burning
 321 velocity with this modified the flame speed method, S_n is plotted against α down to zero, and the mean value of
 322 $\bar{\rho}_b$ evaluated throughout the period of developed, stretched, stable propagation. Equation (5) is then applied to the

323 value of S , except that now the relevant density becomes $\bar{\rho}_b$. Flame speed values of, u_{la} , determined in this way,
324 designated u_{ls} , are closer to those of the PIV values of u_l at zero stretch rate than those based on ρ_b .

325 The values of α_{cl} , below which the flame becomes unstable, are shown for n -butanol /air at different φ , at 0.1
326 MPa and 383 K in Fig. 9. The associated PIV based limiting stable values of u_{nr} at this stretch rate are also shown.
327 At lower values of α_{cl} , flames become unstable and faster burning. The filled square symbols and dotted curve
328 shows the stretch-free values, u_{ls} , derived from this modified flame speed method, allowing for $\bar{\rho}_b$ and Le . These
329 are higher than those of u_{nr} . The lower values of Markstein numbers on the rich side, see Section 5.2, contribute
330 to higher u_{nr} values there.

331 4.4. Radiative heat loss

332 The flame speed method of measuring u_{la} employs the adiabatic values of both density, ρ_b , and temperature, T_b ,
333 with no inherent allowance for either strain rate changes in $\bar{\rho}_b$, or those due to radiative energy loss. The PIV
334 method has no such restrictive assumptions and the associated changes in the burning velocity are embodied in
335 the measurements of S_n and u_g . Radiative heat loss in laminar flames has been computed by several researchers.
336 Zheng Chen et al. [26], found u_{la} for CH₄/air mixtures, to be reduced by the radiation, and decreased by up to 5%
337 and 4% for $\varphi = 0.6$ and 1.4, respectively. For completeness, mathematical modeling of laminar flames requires
338 the effects of flame stretching and radiative energy loss or gain to be included, along with the detailed chemical
339 kinetics and flow patterns. Such modelling shows radiative heat loss to decrease the burning velocity. The decrease
340 in temperature slows the propagation rate, and the burned gas cooling generates an inwards flow [27]. Santner et
341 al. [28] have shown that in an atmospheric heptane/air flame, reductions in burning velocities due to radiative
342 energy loss are less than 1% between $\varphi = 0.9$ and 1.5. Reductions increase as the lean and rich flammability limits
343 are approached.

344 Based on their chemical kinetic modelling, Hao Yu et al. [29] have presented generalised empirical expressions
345 for the reductions in burning velocities of hydrocarbon /air mixtures, as a result of this energy loss under a variety
346 of conditions. The measured burning velocities were subjected to radiative loss. In [29] these losses were
347 calculated for seven different fuels, at different temperatures and pressures. The authors mentioned that this
348 empirical correlation could be used with other fuel/air mixtures, except diluted mixtures. This approach was
349 adopted in the present work and losses were calculated as in [29], and added to the PIV values of u_l at $\alpha = 0$ for
350 the different mixtures. To demonstrate what the hypothetical value of burning velocity would be like in the
351 absence of radiative loss, the calculated loss in burning velocity was added to u_l to give u_{lr} .

352 **5. Discussion**

353 *5.1. Values of laminar burning velocity*

354 The increases in values of u_l to u_{lr} , in the absence of radiative loss, are shown by the filled triangles on the
 355 ensuing Figs. 10-13. These are expressed as % increases in the first column of Table 1. This Table covers three
 356 different aspects of the full range of mixtures, at atmospheric pressure. The second column shows the K_{cl} values,
 357 marking the onset of instability, whilst the third shows the increases in u_{la} to u_{ls} that occur with the revised flame
 358 speed method of processing.

359 **Table 1.** Extent of Radiative Loss, Critical Karlovitz numbers, and Strain Rate/ Le Flame Speed corrections at
 360 atmospheric pressure.

ϕ	Radiative loss % Increase in PIV u_l with no radiative loss				Critical Karlovitz number ($K_{cl} \times 10^3$)				Flame Speed Method % Increase in u_{la} to u_{ls} due to strain/ Le			
	CH ₄	<i>i</i> -C ₈ H ₁₈	C ₂ H ₅ OH	<i>n</i> -C ₄ H ₉ OH	CH ₄	<i>i</i> -C ₈ H ₁₈	C ₂ H ₅ OH	<i>n</i> -C ₄ H ₉ OH	CH ₄	<i>i</i> -C ₈ H ₁₈	C ₂ H ₅ OH	<i>n</i> -C ₄ H ₉ OH
0.7	3.1			1.8	37.8			22.4	-0.9			3.1
0.8	2.0	1.5	1.1	1.5	32.1	9.4	7.9	21.2	-0.9	1.8	1.1	5.0
0.9	1.6	1.4	1.0	1.2	18.5	11.6	6.8	20.0	-0.9	1.6	1.1	4.2
1.0	1.4	1.3	0.9	1.1	15.4	12.4	8.2	17.4	-0.5	1.4	1.8	6.2
1.1	1.4	1.3	0.9	1.0	22.3	13.1	8.9	21.7	1.1	2.7	1.4	5.0
1.2	1.6	1.4	0.9	1.0	25.2	14.3	9.5	25.6	1.0	2.3	1.3	4.3
1.3	2.1	1.7	1.0	1.1	37.7	18.2	10.3	26.7	1.1	3.2	3.6	7.3

361 Although a stable, un-stretched, flame is an unrealistic concept, the complementary values of u_l provide a useful
 362 datum which, along with, Markstein numbers, provides realistic mass burning velocities within the stable flame
 363 regime. Such stretch-free values of laminar burning velocities are shown as a function of ϕ for different fuels in
 364 Figs. 10-13. Full line curves, and cross symbols, show PIV values of u_l , based on u_n . Broken curves, and circle
 365 symbols, show flame speed method values, u_{la} , based on S_n values from the PIV measurements, extrapolated
 366 to $\alpha = 0$, and employing ρ_b in Eq. (5). Values of u_{ls} at $\alpha = 0$, derived from the alternative flame speed method,
 367 based on $\bar{\rho}_b$ and Le , are shown by the filled square symbols. These values are higher than those of u_{la} , values of
 368 the original, broken curve, flame speed method. They are almost equal to the u_l values of the PIV method. These
 369 increases are given in the final column of Table 1. Some of the highest values of u_l are given by the u_{lr} , filled
 370 triangles, with no radiative loss.

371 Figure 10 for CH₄/air mixtures, over a wide range of equivalence ratios at 300 K and 0.1 MPa, presents PIV values
 372 of u_l and ρ_b -based flame speeds values of u_{la} . Points for u_{ls} and u_{lr} also are shown. Values of Le for lean
 373 mixtures range from 0.96 to 0.99, and for rich mixtures it is 1.1 [23, 24]. Because values of Le are close to unity,
 374 the u_{ls} correction is small. The closeness of the u_l and u_{ls} curves indicates the near equality of $\bar{\rho}_b$ from the former
 375 and ρ_b from the latter. The increases in PIV values due to the elimination of radiative loss, indicated by u_{lr} , also
 376 are rather small. There is close agreement between the two methods, although the u_l values, are always higher.
 377 This is because the strain rate correction is small, and there is negligible correction for an increase in the value
 378 of $\bar{\rho}_b$ due to the small radiative cooling. Allowance for this could bring the values of u_l and u_{la} closer together.
 379 Values of u_{la} from other workers also are shown. The values from [32] are noticeably higher. This might be due
 380 to the pressure being recorded, in the absence of flame photographs, and a lack of coordination in flame front
 381 imaging and pressure measurement [35].

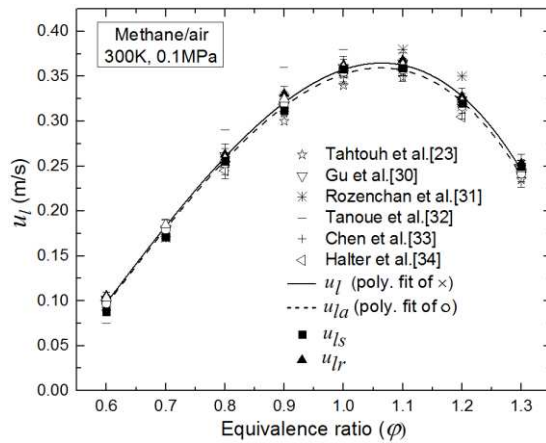


Fig. 10. Unstretched laminar burning velocities, u_l , u_{la} , u_{ls} and u_{lr} for methane/air mixtures at 0.1 MPa and 300 K. Shown also data from literature.

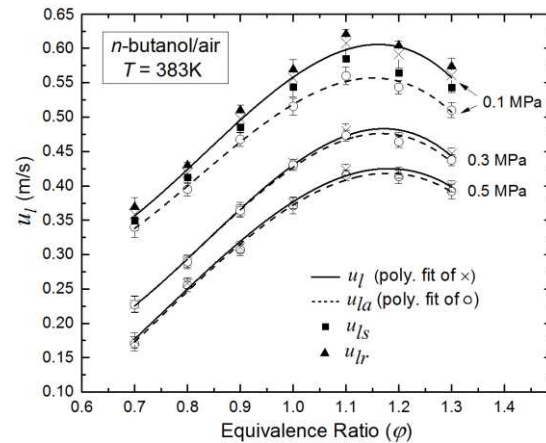


Fig. 11. Unstretched laminar burning velocities, u_l , u_{la} , u_{ls} and u_{lr} for n -butanol/air mixtures at 383 K and different pressures.

382 Figure 11 shows unstretched burning velocities for n -C₄H₉OH, the fuel chosen to study the effects of pressure
 383 changes. Values of Le ranged from 1.35 to 2.1 [25], at 0.1 MPa. The high values of Le create the largest strain
 384 rate corrections. Here, the flame speed values, u_{la} , at 0.1 MPa are 4-11% lower than the PIV values, u_l , with
 385 greater differences for the rich mixtures. Values of all the burning velocities fall with increasing pressure, but
 386 always the u_l values are higher. At 0.1 MPa when the, u_{la} , values are corrected for strain rate and Le , the, u_{ls} ,
 387 values are closer to the u_l values as shown by the filled square points. Allowance for the radiative loss, at 0.1
 388 MPa, results in the u_{lr} values being the highest. Of particular interest is the narrowing of the difference between
 389 the PIV values of u_l and flame speed values of u_{la} with increasing pressure. This can be attributed to values of

390 $\bar{\rho}_b$ approaching those of ρ_b with increasing pressure, as a result of both the more rapid attainment of equilibrium,
 391 and the decreasing values of Le with increasing pressure, see Fig. 8.

392 Figure 12 shows the unstretched burning velocities u_l and u_{la} for *i*-octane/air mixtures at 0.1 MPa and 358 K.
 393 The u_{la} values are underestimates, with a maximum difference of 6.5% below the u_l values. There is rather more
 394 consistency in the atmospheric data for ethanol/air values in Fig. 13. Again, the present results follow a decreasing
 395 trend from u_{lr} down to the u_{la} flame speed method based on ρ_b . Table 1 shows ethanol to have the lowest radiative
 396 energy loss, and its influence is clearly shown by the filled triangles. The original flame speed method
 397 underestimates u_{la} , with a maximum difference of 4.5% with PIV values of u_l .

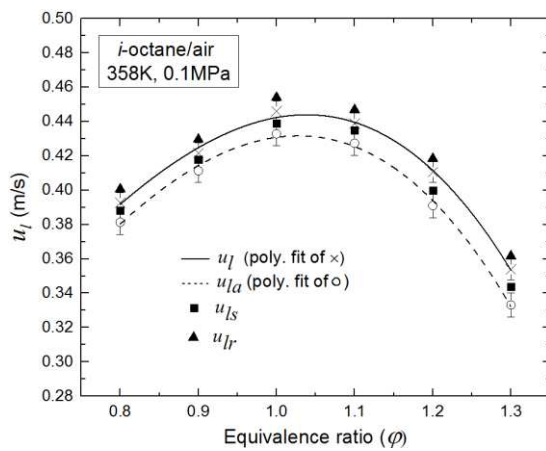


Fig. 12. Unstretched laminar burning velocities, u_l , u_{la} , u_{ls} and u_{lr} for *i*-octane/air mixtures at 0.1 MPa and 358 K.

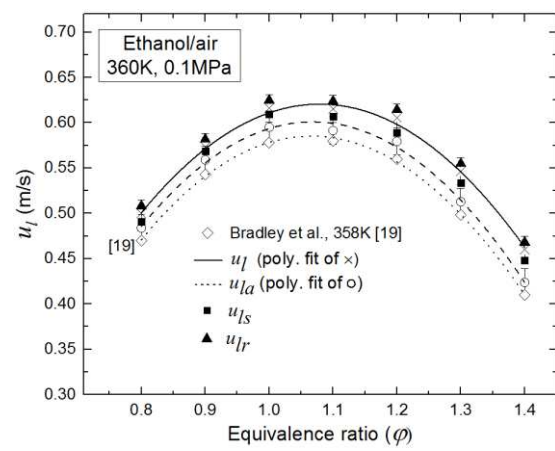


Fig. 13. Unstretched laminar burning velocities, u_l , u_{la} , u_{ls} and u_{lr} for ethanol/air mixtures at 0.1 MPa and 360 K. Shown also data from literature.

398 5.2 Values of Markstein numbers

399 With regard to Markstein numbers, all Markstein lengths, based on both S_n and u_{nr} , were found and normalised
 400 by the flame thickness, δ . The link between Le and Ma is provided by the early expression of Clavin [9]:

$$401 \quad Ma = \frac{1}{\gamma} \ln \frac{1}{1-\gamma} + \frac{\beta(Le-1)}{2} \left(\frac{1-\gamma}{\gamma} \right) x \int_0^{\gamma/1-\gamma} dx \frac{\ln(1+x)}{x}. \quad (11)$$

402 With K_s and K_c expressing Karlovitz strain, $\delta\alpha_{sr}/u_l$ and curvature, $\delta\alpha_{cr}/u_l$, numbers, a practical form of Eq. (8)
 403 is:

$$404 \quad \frac{u_l - u_{nr}}{u_l} = K_s Ma_{sr} + K_c Ma_{cr}. \quad (12)$$

405 The method of deriving the Markstein lengths from the PIV data is given in Section 4.2. Contrasting Markstein
 406 numbers are shown for different ϕ in Fig.14 for methane/air at 0.1 MPa and in Fig. 15 for *n*-butanol/air at 0.1, 0.3
 407 and 0.5 MPa. For CH₄/air the influence of small values of Le close to unity has been discussed in Section 5.1.
 408 With lean mixtures, values of Le are less than unity, leading to the low Markstein numbers in Fig.14. In contrast,

409 for $n\text{-C}_4\text{H}_9\text{OH}/\text{air}$, with richer mixtures, and O_2 as the minority species, the resulting higher diffusion coefficients
 410 creates smaller Lewis numbers, leading to the lower Markstein numbers of Fig.15. With regard to the influence
 411 of pressure, Le decreases with increasing pressure, and this leads to the associated decreasing values of both Ma_{sr}
 412 and Ma_{cr} in Fig. 15.

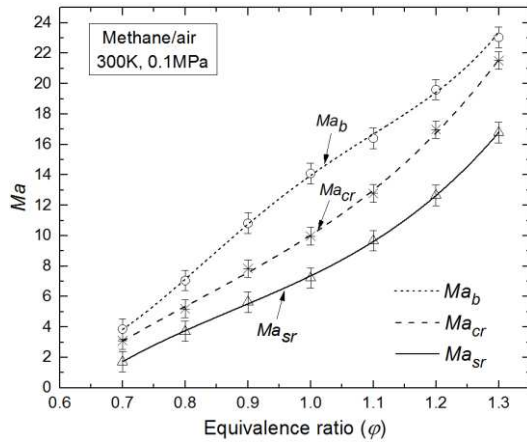


Fig. 14. Variations of Ma_b , Ma_{sr} and Ma_{cr} with ϕ for methane/air mixtures at 300 K and 0.1 MPa.

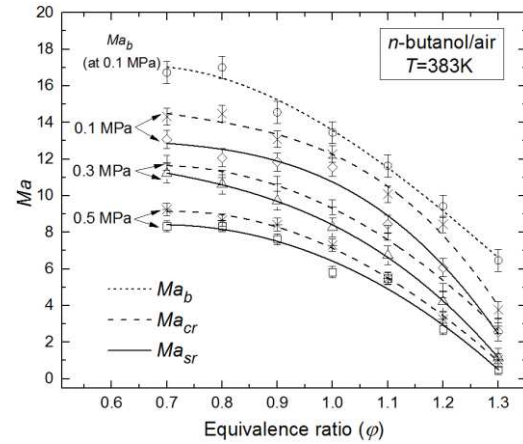


Fig. 15. Variations of Ma_{cr} and Ma_{sr} with ϕ for n -butanol/air mixtures at different pressures and 383 K.

413 Values of Markstein numbers for all the other mixtures studied are tabulated in the supplementary material [S3].
 414 There is a significantly greater spread in the reported values of Markstein numbers than in those of burning
 415 velocities. This is probably inevitable, due to the problem of evaluating a flame thickness, which is defined by
 416 asymptotic end values. Also there are at least three algebraic expressions for flame thickness [36]. In addition, see
 417 Section 4.1, there is a probability of up 4-12% underestimation, depending upon the mixture, in the values of L_b .
 418 In the present study this is a consequence of the low temperature, 570 K, for the stretch rate isotherm. This degree
 419 of underestimation would extend to the different Markstein numbers. Figure 16 shows the measured values of L_b
 420 for CH_4/air at 300 K and 0.1 MPa that are referenced in the present paper. These were predominantly determined
 421 from the uncorrected flame speed method.

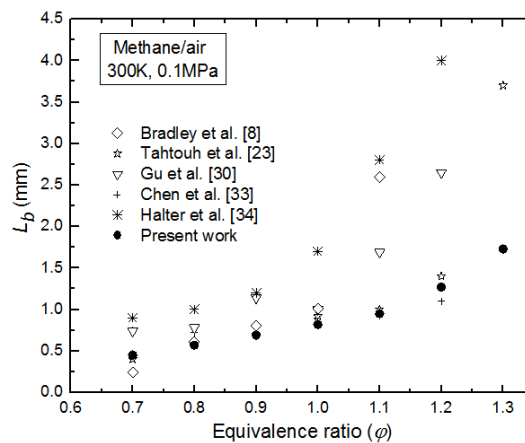


Fig. 16. Flame speed Markstein length, L_b , for methane/air mixtures at 300 K and 0.1 MPa.

424 **6. Conclusions**

425 (i). Stretch-free u_{la} and u_l values have been derived from both flame speed and PIV measurements, respectively.
426 These are valuable, along with Markstein numbers, in expressing practical mass burning velocities, in the stable,
427 stretched flame, regime at stretch rates greater than the critical stretch rate, α_{cl} . They are no guide to the burn
428 rate of developing, unstable, cellular flames at the lower stretch rates.

429 (ii). Values of u_{la} , u_l , u_{ls} , u_{lr} , u_{nr} , Markstein numbers, α_{cl} , and K_{cl} have been found over a full range of φ for
430 methane, *n*-butanol, *i*-octane and ethanol mixtures with air. Effects of pressure have been studied for *n*-butanol/air
431 mixtures.

432 (iii) The flame speed method of measuring unstretched laminar burning velocity, u_{la} , requires the burned gas
433 density to be known and this is usually assumed to be that of burned gas at equilibrium. In practice, the density is
434 increased by the strain rate and Lewis number during stable propagation, and allowance has to be made for this.
435 This brings such flame speed-derived values of u_{ls} into closer proximity to the PIV-derived values, u_l . This stable
436 stretched flame approach is recommended, in preference to the assumption of adiabatic equilibrium for the burned
437 gas density.

438 (iv). PIV measurements provide reasonably accurate values of mass burning rate velocities, along with strain rate
439 and curvature Markstein numbers. Greater errors and general variability arise in the measurement of Markstein
440 lengths, due to stretch rate measurements at different isotherms, with higher temperatures preferred. It is estimated
441 that, on this account, the present values of L_b should possibly be increased by between 4 and 12%. Expressions
442 for laminar flame thickness should always be given.

443 (v). Burning velocity measurements under atmospheric conditions have the aspect of natural phenomena, but
444 corresponding values obtained by mathematical modelling must include the effects of radiative energy loss.
445 Decreases in burning velocities due to radiative energy loss to surroundings at atmospheric temperature are
446 indicated by the differences between the u_{lr} and PIV values of u_l . More generally, radiative energy exchanges
447 might involve energy gain from surroundings at elevated temperatures. Effects of both radiative energy gains and
448 losses in large scale spherical flame propagation are presented in [37].

449 **Acknowledgements**

450 M.E.M thanks the British Council, the Egyptian Cultural and Educational Bureau and the University of Helwan
451 for the financial support of his research. Richard Mumby is thanked for his measurements of schlieren flame
452 speeds.

453 **References**

- 454 [1] Andrews GE, Bradley D. Determination of burning velocities - a critical review. *Combust. Flame* 18 (1972)
455 133-153. [https://doi.org/10.1016/S0010-2180\(72\)80234-7](https://doi.org/10.1016/S0010-2180(72)80234-7).
- 456 [2] Lindow R. An improved burner method for determining laminar flame velocity of fuel gas/air mixtures.
457 *Brenst- Warne-Kraft* 20(1) (1968) 8.
- 458 [3] Bradley D, Hundy GF. Burning velocities of methane-air mixtures using hot wire anemometers in closed
459 vessel explosions. *Symp. (Int.) Combust.* 13 (1971) 575-583. [https://doi.org/10.1016/S0082-](https://doi.org/10.1016/S0082-0784(71)80059-0)
460 [0784\(71\)80059-0](https://doi.org/10.1016/S0082-0784(71)80059-0).
- 461 [4] Jayachandran J, Zhao R, Egolfopoulos FN. Determination of laminar flame speeds using stagnation and
462 spherically expanding flames: molecular transport and radiation effects. *Combust. Flame* (2014) 2305–2316.
463 <https://doi.org/10.1016/j.combustflame.2014.03.009>.
- 464 [5] Yufei Dong, Vagelopoulos CM, Spedding GR, Egolfopoulos FN. Measurement of laminar flame speeds
465 through digital particle image velocimetry: mixtures of methane and ethane with hydrogen, oxygen, nitrogen,
466 and helium. *Proc. Combust. Inst.* 29(2) (2002) 1419-1426. [https://doi.org/10.1016/S1540-7489\(02\)80174-2](https://doi.org/10.1016/S1540-7489(02)80174-2).
- 467 [6] Balusamy S, Cessou A, Lecordier B. Direct measurement of local instantaneous laminar burning velocity by
468 a new PIV algorithm. *Exp. Fluids* 50(4) (2011) 1109-1121. <https://doi.org/10.1007/s00348-010-1027-5>.
- 469 [7] Varea E, Modica V, Vandel A, Renou B. Measurement of laminar burning velocity and Markstein length
470 relative to fresh gases using a new postprocessing procedure: Application to laminar spherical flames for
471 methane, ethanol and isooctane/air mixtures. *Combust. Flame* 159 (2) (2012) 577-590.
472 <https://doi.org/10.1016/j.combustflame.2011.09.002>.
- 473 [8] Bradley D, Gaskell PH, Xiaojun Gu. Burning velocities, Markstein lengths, and flame quenching for
474 spherical methane-air flames: a computational study. *Combust. Flame* 104 (1996) 176-198.
475 [https://doi.org/10.1016/0010-2180\(95\)00115-8](https://doi.org/10.1016/0010-2180(95)00115-8).
- 476 [9] Clavin P. Dynamics behavior of premixed flame fronts in laminar and turbulent flows. *Prog. Energy*
477 *Combust. Sci.* 11 (1985) 1-59. [https://doi.org/10.1016/0360-1285\(85\)90012-7](https://doi.org/10.1016/0360-1285(85)90012-7).
- 478 [10] Bradley D, Mitcheson A. Mathematical solutions for explosions in spherical vessels. *Combust. Flame* 26
479 (1976) 201-217. [https://doi.org/10.1016/0010-2180\(76\)90072-9](https://doi.org/10.1016/0010-2180(76)90072-9).
- 480 [11] Bonhomme A, Selle L, Poinot T. Curvature and confinement effects for flame speed measurements in
481 laminar spherical and cylindrical flames. *Combust. Flame* 160 (2013) 1208-1214.
482 <https://doi.org/10.1016/j.combustflame.2013.02.003>.

- 483 [12] Morley C, Gaseq: a chemical equilibrium program, Ver. 0.79 (2005).
- 484 [13] Giannakopoulos GK, Gatzoulis A, Frouzakis CE, Matalon M, Tomboulides AG. Consistent definitions of
485 "Flame Displacement Speed" and "Markstein Length" for premixed flame propagation. *Combust. Flame* 162
486 (4) (2015) 1249-1264. <https://doi.org/10.1016/j.combustflame.2014.10.015>.
- 487 [14] Bradley D, Hicks RA, Lawes M, Sheppard CGW, Woolley R. The measurement of laminar burning
488 velocities and Markstein numbers for iso-octane–air and iso-octane–n-heptane–air mixtures at elevated
489 temperatures and pressures in an explosion bomb. *Combust. Flame* 115 (1998)126-144.
490 [https://doi.org/10.1016/S0010-2180\(97\)00349-0](https://doi.org/10.1016/S0010-2180(97)00349-0).
- 491 [15] Dunn-Rankin D, Weinberg F. Location of the *schlieren* image in premixed flames: axially symmetrical
492 refractive index fields. *Combust. Flame* 113(3) (1998) 303-311. [https://doi.org/10.1016/S0010-](https://doi.org/10.1016/S0010-2180(97)00233-2)
493 [2180\(97\)00233-2](https://doi.org/10.1016/S0010-2180(97)00233-2).
- 494 [16] Beeckmann, J, Hesse R, Schaback J, Pitsch H, Varea E, Chaumeix N. Flame propagation speed and
495 Markstein length of spherically expanding flames: Assessment of extrapolation and measurement
496 techniques. *Proc. Combust. Inst.* (2018). <https://doi.org/10.1016/j.proci.2018.08.047>.
- 497 [17] Bechtold JK, Matalon M. Hydrodynamic and diffusion effects on the stability of spherically expanding
498 flames. *Combust. Flame* 67 (1987) 77-90. [https://doi.org/10.1016/0010-2180\(87\)90015-0](https://doi.org/10.1016/0010-2180(87)90015-0).
- 499 [18] Bradley D. Instabilities and flame speeds in large-scale premixed gaseous explosions. *Philos. Trans. Royal*
500 *Soc. A* 357 (1999) 3567-3581. <https://doi.org/10.1098/rsta.1999.0510>.
- 501 [19] Bradley D, Lawes M, Mansour MS. Explosion bomb measurements of ethanol–air laminar gaseous flame
502 characteristics at pressures up to 1.4 MPa. *Combust. Flame* 156 (2009) 1462–1470.
503 <https://doi.org/10.1016/j.combustflame.2009.02.007>.
- 504 [20] Bradley D, Lawes M, Mumby R, Pervez Ahmed. The stability of laminar explosion flames. *Proc. Combust.*
505 *Inst.* (2018). <https://doi.org/10.1016/j.proci.2018.07.067>.
- 506 [21] Clavin P, Williams FA. Effects of molecular diffusion and of thermal expansion on the structure and
507 dynamics of premixed flames in turbulent flows of large scale and low intensity. *J. Fluid Mech.* 116 (1982)
508 251–282. <https://doi.org/10.1017/S0022112082000457>.
- 509 [22] Law CK, Cho P, Mizomoto M, Yoshida H. Flame curvature and preferential diffusion in the burning intensity
510 of bunsen flames. *Symp. (Int.) Combust.* 21 (1986) 1803-1809. [https://doi.org/10.1016/S0082-](https://doi.org/10.1016/S0082-0784(88)80414-4)
511 [0784\(88\)80414-4](https://doi.org/10.1016/S0082-0784(88)80414-4).

- 512 [23] Tahtouh T, Halter F, Mounaïm-Rousselle C. Measurement of laminar burning speeds and Markstein lengths
513 using a novel methodology. *Combust. Flame* 156 (2009) 1735–1743.
514 <https://doi.org/10.1016/j.combustflame.2009.03.013>.
- 515 [24] Lowry W, De Vries J, Krejci M, Petersen E, Serinyel Z, Metcalfe W, Curran H, Bourque G. Laminar flame
516 speed measurements and modeling of pure alkanes and alkane blends at elevated pressures. *J. Eng. Gas Turb.*
517 *Power* 133 (9) (2011). <https://doi:10.1115/GT2010-23050>.
- 518 [25] Qianqian Li, Yu Cheng, Wu Jin, Zhaoyang Chen, Huang Z. Study on the laminar characteristics of ethanol,
519 *n*-butanol and *n*-pentanol flames. *SAE Tech. P.* (2015). <https://doi.org/10.4271/2015-01-1933>.
- 520 [26] Zheng Chen. On the accuracy of laminar flame speeds measured from outwardly propagating spherical
521 flames: methane/air at normal temperature and pressure. *Combust. Flame* 162 (6) (2015) 2442-2453.
522 <https://doi.org/10.1016/j.combustflame.2015.02.012>.
- 523 [27] Zheng Chen. Effects of radiation and compression on propagating spherical flames of methane/air mixtures
524 near the lean flammability limit. *Combust. Flame*, 157 (2010) 2267-2276.
525 <https://doi.org/10.1016/j.combustflame.2010.07.010>.
- 526 [28] Jeffrey Santner, Has FM, Ju Yiguang Dryer FL. Uncertainties in interpretation of high pressure spherical
527 flame propagation rates due to thermal radiation. *Combust. Flame*, 161 (2014) 147-153.
528 <https://doi.org/10.1016/j.combustflame.2013.08.008>.
- 529 [29] Hao Yu, Wang Han, Jeffrey Santner, Xiaolong Gou, Chae Hoon Sohn, Yiguang Ju, Zheng Chen.
530 Radiation-induced uncertainty in laminar flame speed measured from propagating spherical
531 flames. *Combust. Flame* 161(11) (2014) 2815-2824. <https://doi.org/10.1016/j.combustflame.2014.05.012>.
- 532 [30] Xiaojun Gu, Haq MZ, Lawes M, Woolley R. Laminar burning velocity and Markstein lengths of methane–
533 air mixtures. *Combust. Flame* 121 (1-2) (2000) 41– 58. [https://doi.org/10.1016/S0010-2180\(99\)00142-X](https://doi.org/10.1016/S0010-2180(99)00142-X).
- 534 [31] Rozenchan G, Zhu DL, Law CK, Tse SD. Outward propagation, burning velocities, and chemical effects of
535 methane flames up to 60 atm. *Proc. Combust. Inst.* 29 (2) (2002) 1461–1470. [https://doi.org/10.1016/S1540-](https://doi.org/10.1016/S1540-7489(02)80179-1)
536 [7489\(02\)80179-1](https://doi.org/10.1016/S1540-7489(02)80179-1).
- 537 [32] Kimitoshi Tanoue, Fumio Shimada, Toshiro Hamatake. The effects of flame stretch on outwardly
538 propagating flames. *JSME Int. J., Ser. B: Fluids Therm. Eng.* 46 (3) (2003) 416–424
539 <https://doi.org/10.1299/jsmeb.46.416>.

- 540 [33] Zheng Chen, Xiao Qin, Yiguang Ju, Zhenwei Zhao, Marcos Chaos, Dryer FL. High temperature ignition and
541 combustion enhancement by dimethyl ether addition to methane–air mixtures. *Proc. Combust. Inst.* 31 (1)
542 (2007) 1215–1222. <https://doi.org/10.1016/j.proci.2006.07.177>.
- 543 [34] Halter F, Tahtouh T, Mounaïm-Rousselle C. Nonlinear effects of stretch on the flame front propagation.
544 *Combust. Flame* 157 (2010) 1825–1832. <https://doi.org/10.1016/j.combustflame.2010.05.013>.
- 545 [35] Hinton N, Stone R, Cracknell R. Laminar burning velocity measurements in constant volume vessels–
546 reconciliation of flame front imaging and pressure rise methods. *Fuel* 211(2018)446-457.
547 <https://doi.org/10.1016/j.fuel.2017.09.031>.
- 548 [36] Palacios A, Bradley D. Generalised correlations of blow-off and flame quenching for sub-sonic and choked
549 jet flames. *Combust. Flame* 185, (2017) 309–318. <https://doi.org/10.1016/j.combustflame.2017.07.019>.
- 550 [37] Zheng Chen. Effects of radiation on large scale spherical flame propagation. *Combust. Flame* 183 (2017)
551 66-74. <https://doi.org/10.1016/j.combustflame.2017.04.031>.